IEEE Transactions on Robotics (T-RO) paper presented at
2024 IEEE/RSJ International Conference on Intelligent Robots and Systems (IROS)
October 14-18, 2024. Abu Dhabi, UAE

Fiber-Optic Force Sensing of Modular Robotic Skin for Remote and Autonomous Robot Control

Sudong Lee, Jae In Kim, Youngjoon Baek, Dongjune Chang, Jeongseob Lee,
Young Soo Park, Dongjun Lee, and Yong-Lae Park

***Abstract*— Robots have taken the place of human operators in hazardous and challenging jobs requiring high dexterity in manipulation, and robots with skin for force and tactile sensing that mimics the function of mechanoreception in animals will be highly dexterous in performing complex tasks. In this study, we propose the design of modular robotic skin, capable of detecting the magnitude and the location of a contact force simultaneously. Each skin module needs three degrees of freedom in sensing in order to estimate the horizontal and the vertical locations of the contact force as well as its magnitude. Force sensing in the proposed skin is enabled by a custom-designed triangular beam structure underneath the skin cover. A force applied to the skin cover causes the bending of the beam, which is detected by fiber optic strain sensors. The result shows the resolutions of 1.45 N for force estimation and 1.85 mm and 1.91 mm for contact localization in horizontal and vertical directions, respectively. We also demonstrate how the proposed skin can be used for remote and autonomous control of commercial robotic arms equipped with an array of the skin modules.**

I. Introduction

High dexterity, comparable to that of humans, is one of the critical requirements for autonomous robots when it comes to performing intricate manipulation tasks across various domains [1], [2]. Robots are often required to execute complex operations in environments that can be hazardous to humans [3], [4]. To address these challenges, two primary approaches have emerged: teleoperation [5]–[7] and autonomous robotic systems equipped with advanced sensing capabilities. Force and tactile sensing play a crucial role in dexterous manipulation of a robot. These sensors not only provide spatial information on the surroundings but also offer physical feedback to the robot, similar to mechanoreception in biology. This feedback enables the robot to discern its motion when it interacts with the environment [8]–[10]. The significance of force and tactile sensing is further emphasized in challenging environments [11], as it increases the success rate of task completion while minimizing the risk of damaging the robot. Researchers have been working on developing sensors that mimic the behavior of the mechanoreceptors found in human or animal skin [12]–[15].

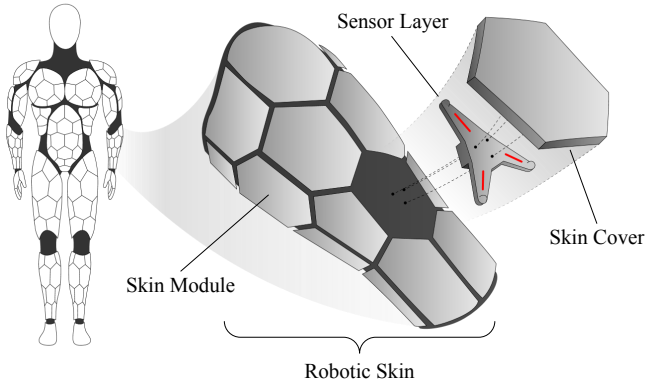

Fig. 1. Conceptual drawing of modularized robotic skin composed of a skin cover and a sensing structure hidden under the cover.

Tactile sensing offers substantial advantages in remote operation, particularly in conveying information on contact locations and objects during manipulation. This feature enables operators to quickly perceive their surroundings and execute precise control tasks. Moreover, it enhances interaction safety by providing the information on contact forces [16]. In autonomous systems, the robot can execute complex tasks reliably, even in the face of unexpected collisions, provided that it can identify the magnitudes and the locations of the contacts in real-time. This capability is important not only for independent task execution but also for seamless collaboration with other robots. Therefore, we propose a new design of robotic skin capable of providing real-time data on contact forces and their locations, facilitating high-level manipulation tasks.

A. Related Work

Tactile sensing is a crucial element in an end-effector functionality and its dexterous manipulation, as discussed in various studies [17]–[22]. However, it is also important in other areas of a robot's body to enhance autonomy, which is

This work was supported in part by the International Nuclear Energy Research Initiative (Grant No.: NRF-2017M2A8A1092482) and in part by the Institute of Information and Communications Technology Planning and Evaluation (IITP) (Grant No.: 2021-0-00896), through the National Research Foundation funded by the Korean Government (MSIT). *(S. Lee and J. I. Kim contributed equally to this work.) (Corresponding author: Y.-L. Park)*

S. Lee was with the Soft Robotics Research Center, Seoul National University, Seoul, Korea. He is now with the CREATE Lab, Institute of Mechanical Engineering, EPFL, Lausanne, Switzerland. (E-mail: sudong.lee@epfl.ch)

J. Kim is with Samsung Electronics, Suwon, Korea. (E-mail: snu08mae@gmail.com)

Y. Baek, J. Lee, D. Lee, and Y.-L. Park are with the Department of Mechanical Engineering; the Institute of Advanced Machines and Design; the Institute of Engineering Research, Seoul National University, Seoul, Korea. (E-mails: {byj4667; overjs94; djlee; ylpark}@snu.ac.kr)

D. Chang is with the Department of Mechanical Engineering, Arizona State University, Tempe, AZ, USA. (E-mail: Dongjune.Chang@asu.edu)

Y. S. Park is with the Argonne National laboratory, Lemont, IL, USA. (E-mail: ypark@anl.gov)

achievable through sensorized skin [12], [23], [24]. This enables robots to efficiently explore their surroundings, reducing operational time and enhancing stability and safety [13], even in dynamic or unknown environments. The real-time data from physical interactions are useful in determining or modifying the body configuration, while tactile sensing skin provides valuable information for planning trajectory [25], [26] and complementing visual feedback from optical systems, such as cameras and lidars [27].

Several research groups have focused on developing various types of tactile sensors for robots using different methods, including room-temperature liquid metals, conductive fabrics, air pressure sensing, hall-effect sensing, proximity sensing, capacitive sensing, vision sensing, electron tomography, and fiber-optic fiber sensing [13], [14], [28], [29].

The liquid-metal sensor detects external forces by monitoring the change in resistance of liquid-filled microchannels embedded in an elastomer matrix, as the channel changes its shape based on the deformation of the structure when external forces are applied [15]. Similarly, the electrical resistance of conductive fabrics varies with surface pressure [30]. Air pressure sensing detects pressure changes resulting from volume reduction in a chamber when forces are applied [31]. Although these mechanisms are soft and easy to attach to the robot's surface, they may not withstand harsh environments where high impact forces are present or do not always provide high accuracy in tactile sensing due to undesired effects, such as hysteresis and creep.

Hall-effect sensing detects change in magnetic field when an external force displaces a nearby magnet relative to the sensor [32], [33]. Vision sensing mechanisms observe structural changes induced by external forces through cameras [34]–[37]. Contact forces can be detected by electron tomography by monitoring changes in impedance or capacitance within the electrical network [38], [39]. Proximity sensors [14], [28] or capacitance sensors can be also used [40], [41]. However, it should be noted that these mechanisms may require additional devices for shielding or noise reduction in harsh environmental conditions, such as electromagnetic interference (EMI) or radiation, as they rely on semiconductors and electric circuits.

Alternatively, fiber-optic sensing is highly accurate and robust, even in harsh environments, especially in challenging environments, since they are electrically passive. This makes it an ideal solution for applications where robot failure or task malfunctions in such environments can be costly. Fiber-optic sensing also provides a spatial advantage to the design, as it can be achieved in a compact form factor and operate reliably in radiation environments without additional shielding. Consequently, many studies have focused on developing tactile sensors for robots using fiber optics [42]–[44].

B. Proposed Approach

In this paper, we propose modularized robotic skin (Fig. 1) equipped with force-sensing capabilities, achieved through fiber optic strain sensors known as fiber Bragg gratings (FBGs) [45], [46], which are strategically embedded within the sensor layer, as shown in Fig. 2(a) [47]. The connection between the skin cover and the sensor layer is established via a joint layer, employing custom-designed joints, called spherical-linear (S-L) joints. These S-L joints allow displacement of the skin cover with three degrees of freedom (DoFs): one for translation and two for rotation. This three-DoF motion enables model-based estimation of both the location and the magnitude of the contact force applied to the skin. Unlike sensors with FBG arrays for discrete estimation of the contact forces [48], the proposed robotic skin allows for continuous estimation of contact force locations.

FBG-based force sensing provides an ideal solution for this application due to several key advantages. First, fiber optics are compact, flexible, and lightweight, and thus easy to embed in structures of complex geometries. Furthermore, FBGs are not only highly sensitive to strain for force sensing but also immune to electromagnetic noise and radiations [49]–[51], providing a potential in robotics applications, including tactile sensing [48], [52], robotic grippers [8], [20], [29], manipulators [53], [54], and medical devices [51], [55], [56]. Moreover, the multiplexing capability of FBGs [57]–[59] makes the system simple, even when employing a large number of sensors [51]. A single optical fiber with multiple FBGs can detect multiple local strains, allowing the sensing system to simultaneously acquire data from many skin modules using just one data acquisition device. FBGs are also capable of long-distance sensing [60] and effectively shielding electrical components from harsh environmental conditions, making themselves less susceptible to electromagnetic interference (EMI) and radiation.

C. Contributions

The modular design of the robotic skin offers several advantages. First, it enhances versatility by facilitating easy integration with existing robotic structures of varying shapes and sizes [61]. This adaptability allows for the application of the skin to a wide range of robotic systems. Another advantage is easy repair of the skin with failures, since it allows for partial replacement of failure modules [13], which reduces the repair cost as well as the time. Furthermore, the modular design enables multi-touch sensing capabilities. In conventional robotic systems equipped with multi-axis force-torque sensors, typically located at the wrist joint [62], [63], the ability to distinguish multiple simultaneous contacts is limited. They can only process multiple forces as a single lumped force at the end-effector, thereby constraining their practicality for autonomous robotic applications. In contrast, in our approach, since each skin module estimates the force applied to itself individually, the entire skin is able to process the information on the multiple forces simultaneously.

D. Result and Contents

Our prototype of the proposed robotic skin showed the resolutions of $1.85\,\mathrm{mm}$ and $1.91\,\mathrm{mm}$ for localization in lateral and longitudinal directions, respectively, and $1.45\,\mathrm{N}$ for force estimation. We were able to achieve a sensing bandwidth higher than $850\,\mathrm{Hz}$ through modeling and parameter optimization.

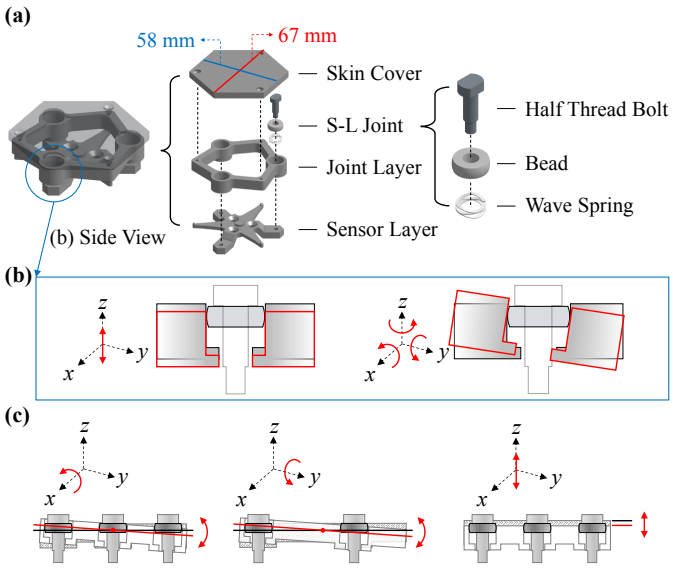

Fig. 2. (a) Components of the skin module with dimensions. (b) Four-DoF motions of the S-L joint. (c) Three-DoF motions in the skin module. The skin module has roll, pitch, and z-axis translation motions.

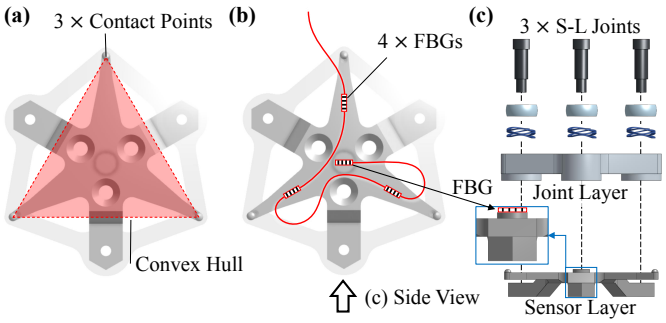

Fig. 3. (a) Three contact points form the convex hull of a triangle. (b) Layout of four FBGs on the sensor layer. Three FBGs attached on the beam are for force sensing and one at the center for temperature compensation. (c) Side view of the skin module without the skin cover and the magnified view of the sensor layer center position.

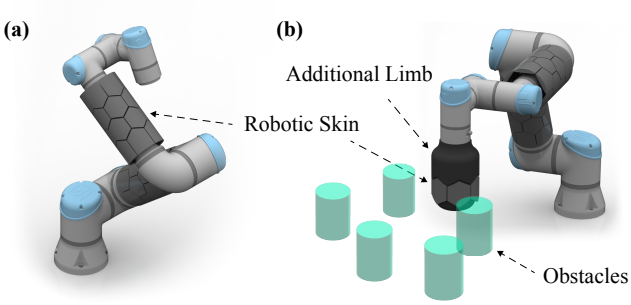

Fig. 4. (a) Each link of an industrial robot arm with multiple skin modules. (b) Additional link with robotic skin added to the distal end of the arm.

The rest of this paper is organized as follows. In Section II, we describes the design concept, key features, and fabrication process of the skin modules, along with considerations for an arrayed skin structure. Section III explains the modeling of the skin structure for force sensing, incorporating beam theory, and discusses the continuous estimation of contact force locations and magnitudes based on the modeling results. Section IV presents the results of the skin module characterization. Section V demonstrates the applications of our robotic skin, particularly in remote operation and autonomous control of a robotic arm. Section VI discusses the contribution of our skin and future work, and Section VII finally concludes the work.

II. Design

The robotic skin is a combination of hexagonal grids and can easily cover a curved surface. Each grid is called as a skin module in our design, and the top layer (i.e., skin cover) of each module was designed to have three-DoF motions in order to obtain three pieces of force information (the magnitude and the locations in x- and y-axes). The skin module consists of four components: a skin cover, a joint layer, three spherical-linear (S-L) joints, and a sensor layer.

A. Skin Module

1) Sensor Layer: The sensor layer is the base of the skin module, composed of a triangular beam structure and three wings with screw holes, as shown in Fig. 3(a). Each beam has a small protrusion at the end, making a contact with the joint layer. A force applied to the skin cover combined with the joint layer is transmitted to the sensor layer only through these three points, and bending of the three beams allows for detection of the force with three DoFs. In other words, the strain changes of the three beams provide enough information to find out the location and the magnitude of the force. Each beam has an FBG bonded on top, which measures the strain changes of the beam, as shown in Fig. 3(b). Since each FBG had its own length (approximately $3\,\mathrm{mm}$) and uniform strains needed to be applied over the area where the FBG was bonded, the beam was designed to have a tapered shape. To compensate for temperature effects, a fourth FBG was bonded at the center of the beam structure, in addition to the FBGs on the beams. To minimize the strain change at the center area, fixed parts were added between the center and the deformed beams with three bolts. Moreover, the height difference of the center reduced stress concentration at the line where the surface angle changed to $90°$, which minimized the strain change on the FBG attachment area. As a result, the strain change at the center area was negligible and affected only by the temperature.

2) Joint Layer: The joint layer, which connects the sensor layer and the skin cover, has three cylindrical sockets. Each socket holds a S-L joint composed of a large-hole bead, a wave spring, and a half threaded bolt. The bead allows four-DoF motions of the joint layer, such as vertical translation and rotations about three axes, as shown in Fig. 2(b) that shows possible movements near the one S-L joint. In order to achieve three DoFs in a skin module, three S-L joints were used at $120°$ intervals. Although each joint has four DoFs individually, the sensor layer fixed at the bottom constrains the yaw motion of the joint layer composed of three S-L joints. Therefore, this allowed the skin cover not only to

rotate in x and y axes but also to linearly move in z-axis. Fig. 2(c) shows the resulting three DoFs of the skin module; roll, pitch, and vertical translation.

3) Skin Cover: The skin cover is the outermost layer of the skin module with a hexagonal shape. Hexagons are one of three types of polygons that can cover a large area without leaving gaps when arrayed, making the entire skin easily reconfigurable depending on the size or the shape of the host structure. When a force applied inside the convex hull of the sensor layer, Fig. 3(a), all three corners of the triangle are compressed and causes bending of the beams. However, if a force is applied outside the convex hull but still within the hexagonal area, the farthest corner from the force may lose contact due to the moment of the axis that passes through the other two corners. As a result, the farthest tip of the beam may lose contact with the joint layer, making it difficult to measure the applied force and estimate its location and magnitude. To address this issue, the sensor layer was bolted to the joint layer with prestress, ensuring that contact is maintained. This means that the farthest beam is only relaxed from the prestress instead of losing contact, allowing the three FBGs to detect a force applied anywhere inside the skin cover.

The skin module requires a flat sensor layer, as shown in Fig. 2(a), but the skin cover can be designed with various shapes, including curvatures. Estimation models for distinct geometries can be formulated by considering geometric constraints on the shape. In this paper, we designed and tested skin covers with both a flat and a curved surfaces that can cover a cylindrical robotic arm.

4) Fabrication: All the structures and the components were made of stainless steel by machining. The total weight of a single module is $113\,\mathrm{g}$. For accuracy in sensing, both of the sensor layer and the joint layer were precisely machined to have tolerance of less than $0.01\,\mathrm{mm}$. Also, the beads and the sockets of the joint layer were machined to have bearing tolerance of $0.01\,\mathrm{mm}$, respectively, in order to minimize the friction. In addition, a groove (length: $4\,\mathrm{mm}$) was engraved on each place for an FBG to be bonded on the joint layer using a laser cutter (Speedy 300 Flexx, Trotec, Austria). The FBGs were bonded to the grooves using cyanoacrylate adhesive, as shown in Fig. 3(b). The modules are assembled as the exploded view from the side, shown in Fig 3(c). The width and the depth of a module is $58\,\mathrm{mm}$ and $76\,\mathrm{mm}$, respectively.

B. Skin Array

The skin can be attached to a curved surface by incorporating a structure between the robot and the skin. The design of the skin cover offers considerable flexibility, allowing it to continuously integrate with the robot's surface when affixed, as shown in Fig. 4. In this research, the skin modules can be utilized with industrial robot arms, as shown in Fig. 4(a). The robotic skin is cylindrical following the shape of the robot limb. It consists of multiple rows of six curved skin modules. The hexagonal shape of the module enabled to cover the entire surface area of the arm without leaving any gaps. The skin module can be adjusted in size to enable installation as closely as possible to the surface of the robot, thanks to their scalability. Details on scalability are provided in APPENDIX D. To evaluate the robotic skin, an additional limb covered with a row of skin modules is attached to the end effector (Fig. 4(b)). There exist parallels between Figs. 4(a) and 4(b) in the processing and exploitation of the sensor data for the control of the robotic arm, owing to the similarity in the configuration. Furthermore, the case of Fig. 4(b), which aligns with the application setup of Section V, shows the versatility of the tactile skin by employing all DoFs of the robotic arm.

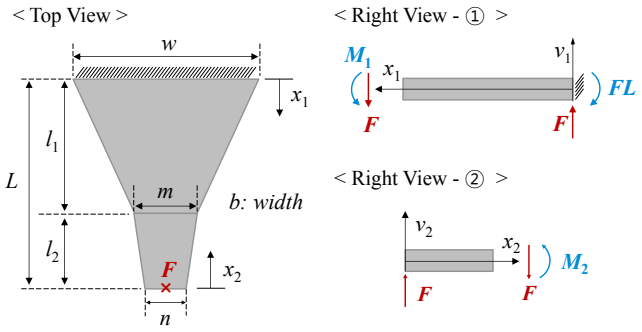

Fig. 5. Model of the tapered beam. The right view 1 is right side of the beam for x_1, and the right view 2 is right side of the beam for x_2.

III. Modeling

A. FBG Sensing Principle and Temperature Compensation

When a light injected into an optical fiber meets an FBG, a specific wavelength of the input light is reflected back to the origin while the rest wavelengths are transmitted to the other side. This specific wavelength is called as a peak wavelength or a Bragg wavelength. The peak wavelength is determined by the grating pitch, Λ, and the effective refractive index, n_{eff}, of the FBG, and their relationship is [64]

$$\lambda_p = 2n_{eff}\Lambda \tag{1}$$

where λ_p is the peak wavelength.

The grating pitch changes by the axial strain applied to the FBG area in the fiber or the temperature change of the FBG. The relative shift of the peak wavelength, $\frac{\Delta\lambda_p}{\lambda_p}$, is given as

$$\frac{\Delta\lambda_p}{\lambda_p} = (1-p_e)\cdot\epsilon + (\alpha_\Lambda + \alpha_\eta)\cdot\Delta T \tag{2}$$

where ϵ is the strain applied to the FBG, p_e is the photo-elastic coefficient, α_Λ is the thermal expansion coefficient, α_η is the thermo-optic coefficient, and ΔT is the temperature change [65]. In order to eliminate the effect of temperature change, Eqn. (2) is subtracted by the relative shift of a peak wavelength that is affected not by strain but only by temperature [20].

B. Tapered Beam

1) Strain of the Beam: A typical cuboid-shaped cantilever beam does not experience uniform strains along its length

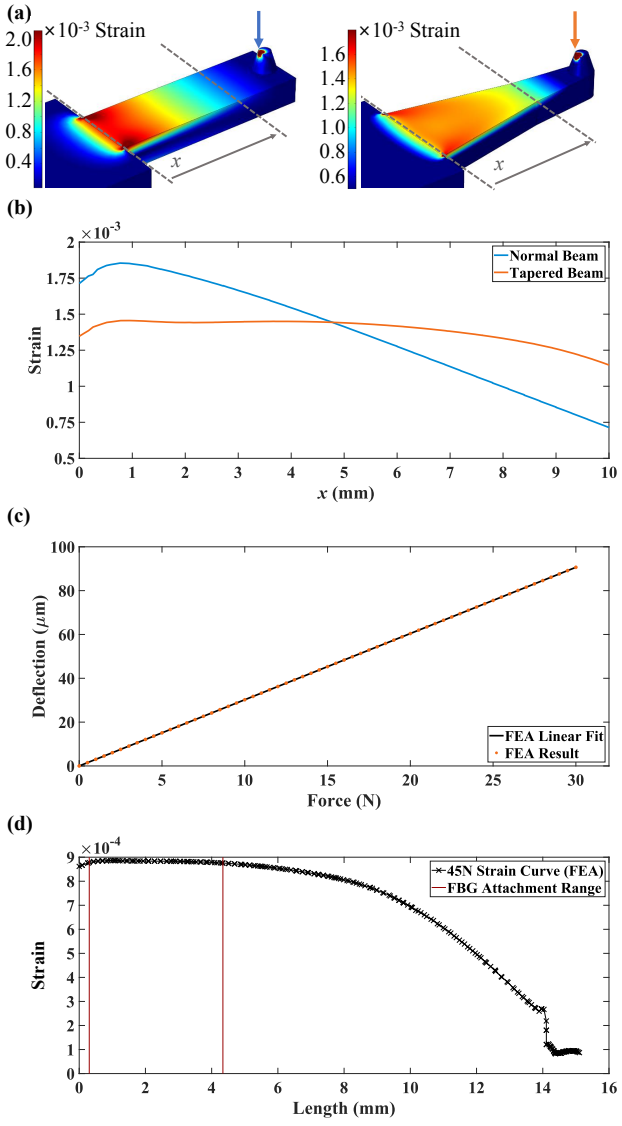

Fig. 6. Comparison of strain profiles of a regular beam and a tapered beam. The strain at the top surface of the regular beam decreases linearly along the length while that of the tapered beam maintains relatively constant. (a) Graphical comparison. (b) Quantitative comparison. (c) Deflection of the tapered beam vs. force (FEA). (d) Strain profile of the tapered beam along the length when a tip force of 45 N was applied. The difference between the maximum and the minimum strains is less than 1.2×10^{-5} between 0.30 mm and 4.34 mm (two red lines).

direction when the beam is bent. If FBGs are attached to the cuboid-shaped cantilever beam, there is a problem that the changing strains cannot be accurately sensed by the FBGs since the FBGs have their own lengths. It will be highly useful if uniform strains can be applied at least to the area to which an FBG is bonded. This will not only reduce the computational cost but also increase the accuracy in strain measurement. Moreover, we do not need to use any special calibration process to find a nominal strain of a section [66]. Therefore, the design of the beam needs to be revised in order to have a constant strain along its length direction. The flexure formula is given as

$$\sigma = E\epsilon = \frac{My}{I},\ I = \frac{bh^3}{12},\ y = \frac{h}{2} \tag{3}$$

where σ is the normal stress, E is the Young's modulus, ϵ is the normal strain, M is the internal moment, y is the vertical distance from the neutral axis, and I, b, and h are the moment of inertia, the width, and the height of the cross-sectional area, respectively [67]. Since M is equal to $F(L-x)$, where F, x, and L are the external force, the horizontal location of the beam, and the length of the beam, respectively, the strain can be expressed as

$$\epsilon = \frac{My}{EI} = \frac{6F(L-x)}{Ebh^2} \tag{4}$$

by using Eqn. (3). If we choose $b = p(L-x)$, where p is an arbitrary real number, the strain (ϵ) finally becomes independent of x as follows

$$\epsilon = \frac{6}{pEh^2}F. \tag{5}$$

The tapered beam was designed based on this concept, as shown in Fig. 5. The width of the beam (b) decreases linearly, but the slope changes at the tip that makes contact with the joint layer as

$$b = \begin{cases} \frac{w}{L}(L-x_1), & \text{if } 0 \le x_1 \le l_1 \\ \frac{m-n}{l_2}x_2 + n, & \text{if } 0 \le x_2 \le l_2. \end{cases} \tag{6}$$

Since the FBG is attached between $0 \le x_1 \le l_1$, the strain (ϵ) can be found as

$$\epsilon = \frac{6L}{wEh^2}F = \frac{F}{K_b},\ K_b = \frac{wEh^2}{6L} \tag{7}$$

where K_b is the proportional constant. Since the force applied to the beam (F) is proportional to the strain (ϵ) the force can be calculated from the strain detected by the FBG.

The strain uniformities of the cuboid-shaped beam and the tapered beam are compared using a finite element analysis (FEA) (COMSOL Multiphysics, Comsol) as shown in Fig. 6(a)-(b). When the same force is applied to beams of the same length, the strain of the cuboid-shaped beam decreases linearly along the length while that of the tapered beam shows much more uniform. According to the strain equation ($\epsilon = F/K_b$), the strain of the tapered beam should be completely flat between $0 \le x_1 \le l_1$, but the FEA result slightly decreases at the base and near $x_1 = l_1$ (In our design, l_1 is 10 mm). This is because stress concentration occurs at the base and the slope of the tapered beam changes at $x_1 = l_1$.

2) Deflection of the Beam: According to the Euler–Bernoulli beam theory, the quadratic differential equations of the deflection of the beam are [67]

$$\begin{aligned} \frac{d^2v_1}{dx_1^2} &= \frac{M_1}{EI_1} \ (\text{if } 0 \le x_1 \le l_1), \\ \frac{d^2v_2}{dx_2^2} &= \frac{M_2}{EI_2} \ (\text{if } 0 \le x_2 \le l_2) \end{aligned} \tag{8}$$

where I_1, M_1, I_2 and M_2 are as follows

$$\begin{aligned} I_1 &= \frac{wh^3(L-x_1)}{12L},\ M_1 = F(L-x_1), \\ I_2 &= \frac{h^3}{12}\left(\frac{m-n}{l_2}x_2 + n\right),\ M_2 = -Fx_2. \end{aligned} \tag{9}$$

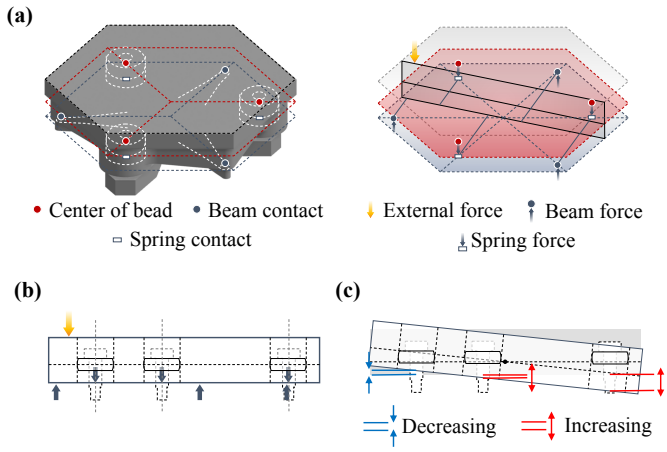

Fig. 7. Model of the skin module. (a) Free body diagram of the joint layer and the skin cover. cross-sectional plane (black solid line) is formed by the center of the skin module and the external force. (b) Free body diagram of the cross-sectional plane. (c) Deformed shape of the module on the cross-sectional plane showing the displacements of the three springs in the S-L joints.

The boundary conditions are

$$\left.\frac{dv_1}{dx_1}\right|_{x_1=0} = 0, \quad \left.\frac{dv_1}{dx_1}\right|_{x_1=l_1} = \left.\frac{dv_2}{dx_2}\right|_{x_2=l_2}, \qquad v_1|_{x_1=0} = 0, \quad v_1|_{x_1=l_1} = v_2|_{x_2=l_2}. \tag{10}$$

Using the quadratic differential equations and the boundary conditions, the deflection of the tapered beam at the tip can be calculated as

$$v = K_v F \tag{11}$$

where K_v is the deflection proportional constant (Details on the beam deflection is written in Appendix A). Since the deflection of the beam at the tip is proportional to the force, the deflection can be calculated from the force. This linearity is also verified by the FEA as shown in Fig. 6(c).

3) Beam Specifications: The maximum sensing force of each beam is $45\,\mathrm{N}$, which is determined by the maximum stress concentrated at the boundary before yielding, based on the FEA result. Also, the minimum sensing force of each beam is $0.62\,\mathrm{N}$, considering the noise level of the FBG interrogator (SI255, Micron Optics, USA), approximately 1.2×10^{-2} nm, which corresponds to 1.2×10^{-5} strain. The FBG attachment section is between $0.30\,\mathrm{mm}$ and $4.34\,\mathrm{mm}$ as shown in Fig. 6(d). When the maximum sensing force is applied at the tip of the beam, the difference between the maximum and the minimum strains is 1.1×10^{-5} strain which is less than the strain corresponding to the noise level of the interrogator. Since the length of each FBGs is designed to be $3\,\mathrm{mm}$, $4.04\,\mathrm{mm}$ is sufficient for attachment when considering the manufacturing tolerance. (The specifications of the FBGs and the interrogator are provided in APPENDIX B.)

C. Spring Force

When a force is applied to the skin cover, the three beams in the sensor layer bend while maintaining the contacts with the joint layer. The three contact points between the beams and the joint layer constitute a beam plane, as shown in Fig. 7(a). Since the FBG outputs tell the state of beam bending, the positions of the three contact points can be obtained using Eqn. (11). Then, the normal vector of the beam plane is

$$\left(\vec{P}_{beam_2} - \vec{P}_{beam_1}\right) \times \left(\vec{P}_{beam_1} - \vec{P}_{beam_3}\right) = \vec{N}_{beam} \tag{12}$$

where $\vec{P}_{beam_1}$, $\vec{P}_{beam_2}$, and $\vec{P}_{beam_3}$ are the position vectors of the contact points, and $\vec{N}_{beam}$ is the normal vector of the beam plane.

The equation of the beam plane is determined by the position of the first beam contact point as

$$\vec{N}_{beam} \cdot (\vec{p} - \vec{P}_{beam_1}) = 0 \tag{13}$$

where $\vec{p}$ is an arbitrary point of the beam plane. The initial position of the bead in each S-L joint is constrained by the wave spring and the bolt head of the joint. When a force is applied to the center of the skin cover, the beads are located below the bolt heads because the joint layer moves down horizontally. If the force is applied to anywhere on the cover except for the center, the joint layer is tilted, as shown in Fig. 7(c). As the joint layer moves, the beads are located along the bolts to satisfy geometric compatibility with the sockets of the joint layer. The vertical displacement of the beads with respect to the beam plane corresponds to the length of the springs in the equation for x and y positions, which can also be related to the changes of the spring forces, $\Delta\vec{F}_{spring,i}$ for $i = 1, 2, 3$. The beam plane equation can be used to find the x, y positions where the spring and the joint layer meet because the bolts constrain the x, y positions of each spring. These positions are expressed as $\vec{P}_{spring,i}$ for $i = 1, 2, 3$.

D. External Force

1) Flat Skin Cover: We assume that the external contact force is applied perpendicular to the surface of the skin cover and the shear force is thus negligible. Fig. 7(b) shows the configuration of the external force, the beam forces, and the spring forces in each skin module. The beam forces can be obtained by Eqn. (7), and prestressed beam forces can also be obtained. Since the skin module needs to achieve a static equilibrium, the sum of the spring force changes and the beam force changes becomes the magnitude of the external force. We can now estimate the magnitude and the location of the external force using a force balance equation and a moment balance equation. The force balance equation is given as

$$\vec{F}_{external} + \sum_{i=1}^{3} \Delta\vec{F}_{beam,i} + \sum_{i=1}^{3} \Delta\vec{F}_{spring,i} = 0 \tag{14}$$

where $\vec{F}_{external}$ is the external forces, $\Delta\vec{F}_{beam,i}$ is the change of each beam force. The moment balance equation

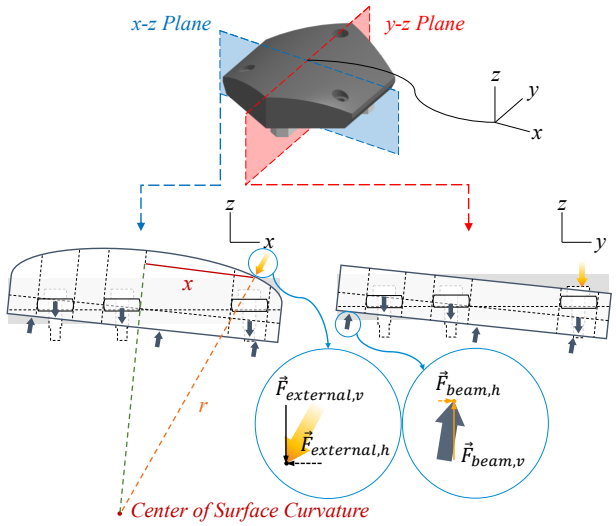

Fig. 8. Model of the curved surface skin module. The left is for x-z plane, and the right is for y-z plane. x is the location of the force in x-axis, and r is the radius of the surface curvature.

is then

$$\left(\vec{P}_{external} \times \vec{F}_{external}\right) + \sum_{i=1}^{3}\left(\vec{P}_{beam,i} \times \Delta\vec{F}_{beam,i}\right) + \sum_{i=1}^{3}\left(\vec{P}_{spring,i} \times \Delta\vec{F}_{spring,i}\right) = 0 \tag{15}$$

where $\vec{P}_{external}$ is the location of the external force. To summarize, all the forces and moments that occur in the skin module are calculated, and then the locations of the external forces are estimated using this information.

2) Curved Skin Cover: In the same way as the flat skin cover modeling, we assume that the external force is perpendicular to the surface of the skin cover and that the shear force is negligible due to the low surface friction. However, it is necessary to consider the surface shape of the skin cover in modeling. To solve this problem, a geometric constraint and additional forces are added to the model.

When modeling a curved surface, an additional lateral component is added to the external force, not present in flat surface modeling. This lateral component causes the force to become perpendicular to the skin cover surface. The skin cover is curved only about y-axis, assuming it covers a cylindrical robotic structure whose axis is parallel with y-axis, as shown in Fig. 8. Thus, the force is composed of only x-z components.

According to Fig. 8, the magnitude of the horizontal component of the force and the force vector are given as

$$\left|\vec{F}_{external,h}\right| = \left|\frac{x}{\sqrt{r^2 - x^2}}\vec{F}_{External,v}\right|, \qquad \vec{F}_{external} = \vec{F}_{external,v} + \vec{F}_{external,h} \tag{16}$$

where $\vec{F}_{external,h}$ is the horizontal component of the external force, x is the location of the force in x-axis, and r is the radius of the surface curvature, which is the same as the radius of the cylindrical robotic skin.

Fig. 8 shows that each beam applies the force perpendicular to the beam plane. Since we can estimate $\vec{F}_{beam,v}$ that is the vertical component of the beam force, the total beam force can be calculated as

$$\vec{F}_{beam} = \frac{\left|\vec{F}_{beam,v}\right|^2}{\vec{F}_{beam,v} \cdot \vec{N}_{beam}}\vec{N}_{beam} \tag{17}$$

where $\vec{N}_{beam}$ is the normal vector of the beam plane.

$\vec{F}_{beam,v}$ and $\vec{N}_{beam}$ can be calculated from Eqn. (7) and Eqn. (12), respectively. $\vec{F}_{spring,v}$ is obtained in the same way as the flat surface modeling. Finally, $\vec{F}_{external,v}$ is given as

$$\vec{F}_{external,v} + \sum_{i=1}^{3}\Delta\vec{F}_{beam,i} + \sum_{i=1}^{3}\Delta\vec{F}_{spring,i} = 0. \tag{18}$$

Since the moment balance equation is equal to Eqn. (15), we can finally find the magnitude and the location of the contact force by solving Eqns. (15) and (16).

3) Line, Surface, or Multiple Forces: The skin module detects the two moments generated by distributed or multiple forces, which are equivalent to the moments produced by the resultant force. The magnitude and the location of the resultant force are the net force and the centroid of the area created by the original forces, respectively. The skin module thus estimates both the magnitude of the net force and the location of the force area's centroid. Although each skin module cannot distinguish multiple external forces, the proposed skin consists of multiple skin modules, and each module can estimate the forces applied to itself simultaneously. Thus, the sensing system can separate and identify each contact point using the information from the skin modules. Moreover, by adjusting the size of each skin module, we can control the spatial resolution of the tactile information from the skin system.

IV. Experiments

We conducted experiments to characterize the proposed system by applying forces to various locations on the skin cover. The estimated magnitude and locations of the forces were compared with the reference values. Parameter optimization was conducted to increase the estimation accuracy.

A. Experimental Setup

Fig. 9(a) shows the setup for experiments. An indenter was combined with a load cell (RFT60-HA01, Robotous, Korea) and attached to a motorized x-y-z stage. Forces were applied to the skin cover by the indenter with a hemispherical tip for point contact with the skin. In the case of the curved skin cover, forces were applied to the skin cover with an angle emulating normal forces, as shown in Fig 8-bottom-left. Fig. 9(b) shows the system configuration and the data flow. The FBG data were collected by the interrogator, and the reference force data were measured by the load cell. The position commands for the x-y-z table were used as the reference location of the force.

For the experiments, forces were applied to the entire area of the skin cover every $2\,\mathrm{mm}$ in both x and y axes

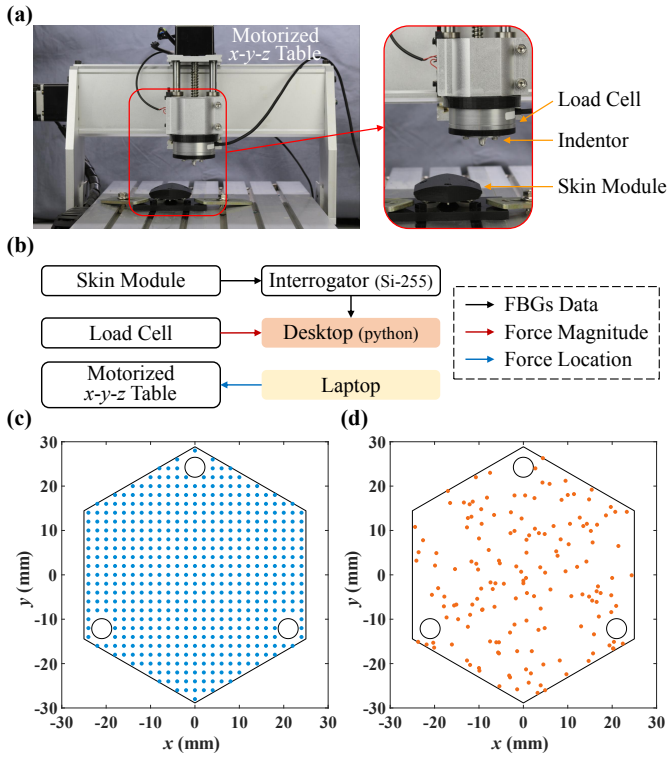

Fig. 9. (a) Experimental setup. (b) System configuration and data flow. (c) Train data and (d) test data of force locations on the skin cover.

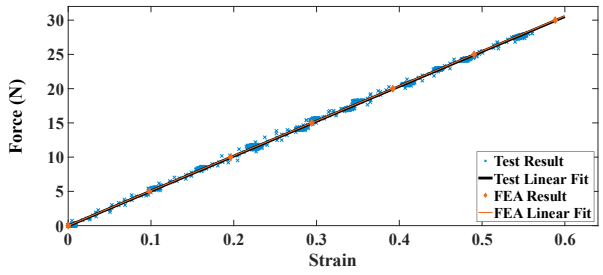

Fig. 10. Comparison between the experimental and the FEA results. The FEA result using the modified Young's modulus is almost identical with the experimental result. Both results show that force is linearly proportional to strain and are the initials value for parameter optimization.

with a grid pattern, as shown in Fig. 9(c). The grid did not include the areas for bolts fixing the skin cover. The force at each location was continuously increased up to the limit and decreased back for collecting train data. The force limit of the skin module was determined by considering the range of elastic deformation of the sensor layer and the safety factor. Additional data were obtained independently by applying external forces to random locations for collecting test data, as shown in Fig. 9(d). The train data were used for parameter optimization, and the test data were used to evaluate the result of the optimization.

B. Initialization

Since the FBG peak wavelength may change depending on the external environment, such as temperature. It is necessary to initialize the sensor outputs at the start of sensing, which can be done by simply subtracting the offset from the outputs. The average of the first 60 FBG data before applying external forces was used to determine the offset value. By processing the data through modeling, the offset values that make the external force closest to zero were numerically obtained.

C. Parameter Optimization

Although we assumed a frictionless condition in modeling, there was actually friction in the S-L joints of the prototype, which prevented full transmission of the force applied to the skin cover to the sensor layer. Therefore, it was necessary to optimize the constants, K_b and K_v, for accurate estimation of the magnitude and position of the beam forces.

The initial values of optimization were obtained by directly applying the forces to the three beams without the skin cover and the joint layer. The constants were optimized using nonlinear least squares method to minimize the difference between the reference and the collected data at $2\,\mathrm{mm}$ intervals. K_b and K_v values for each beam were optimized respectively, and the initial values of K_b and K_v were determined based on the results of Fig. 10. As a result, K_b and K_v were changed by 21.11% and 36.49% in average, respectively.

D. Result

1) Flat Skin Cover: Fig. 11(a)-(c) shows part of the experimental results of estimating the locations and the magnitude of forces applied to the skin cover based on the beam model and the optimized K_b and K_v. The RMSEs for estimating the x and y locations were $1.85\,\mathrm{mm}$ and $1.91\,\mathrm{mm}$, respectively. The RMSE for estimating the magnitude was $1.45\,\mathrm{N}$. The RMSE for increased forces of every $5\,\mathrm{N}$ is plotted in Fig. 11(d). When the magnitude of the force is low (near zero), the accuracy of the location is relatively low. This is because the signal to noise ratio was small in the small force range, and the skin module did not completely return to the initial position due to the friction. The RMSE for increased distances of every $5\,\mathrm{mm}$ from the origin is as shown in Fig. 11(e). The minimum estimated force based on the modeling was $4.3\,\mathrm{N}$ due to the noise level of the interrogator. The result of hysteresis analysis is provided in APPENDIX E.

2) Curved Skin Cover: We also conducted an experiment for the curved skin cover in the same way for the flat skin cover. Fig. 12(a)-(c) shows the results of estimating the locations and the magnitude of forces based on the model of the curved surface and the optimized K_b and K_v. The RMSEs for estimating the x and y locations were $1.80\,\mathrm{mm}$ and $1.67\,\mathrm{mm}$, respectively. The RMSE for the magnitude was $1.74\,\mathrm{N}$. The RMSE for every $5\,\mathrm{N}$ of applied force is shown in Fig. 12(d). When the magnitude of the force is low, the accuracy is relatively low, similar to the result of the flat skin cover. Since the correction for the lateral component of the external force was not perfect, the RMSE for magnitude estimation was relatively high. Friction can be a factor in this scenario, as the movement of the indenter in the z-direction

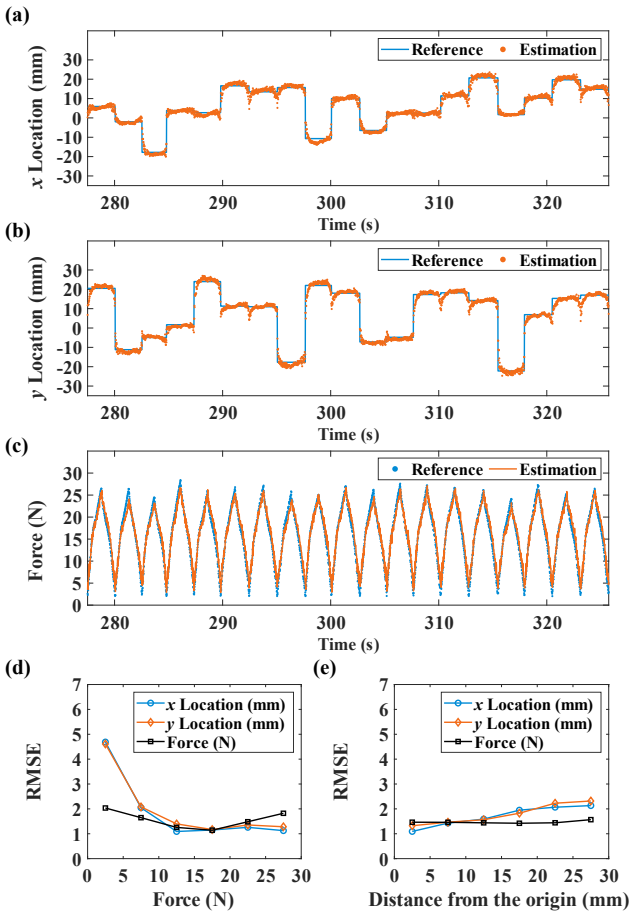

Fig. 11. Experimental results for the flat skin cover: the estimated locations of in (a) x- and (b) y-axis and (c) magnitudes of the applied forces and the RMSE values of the estimations with increments of (d) 5 N of force and (e) 5 mm of displacement. (This part shows various cases among the estimation results.) The RMSE values were evaluated using the test data acquired at random locations shown in Fig. 9(d). Force at each location was continuously increased up to the limit and decreased back to the initial.

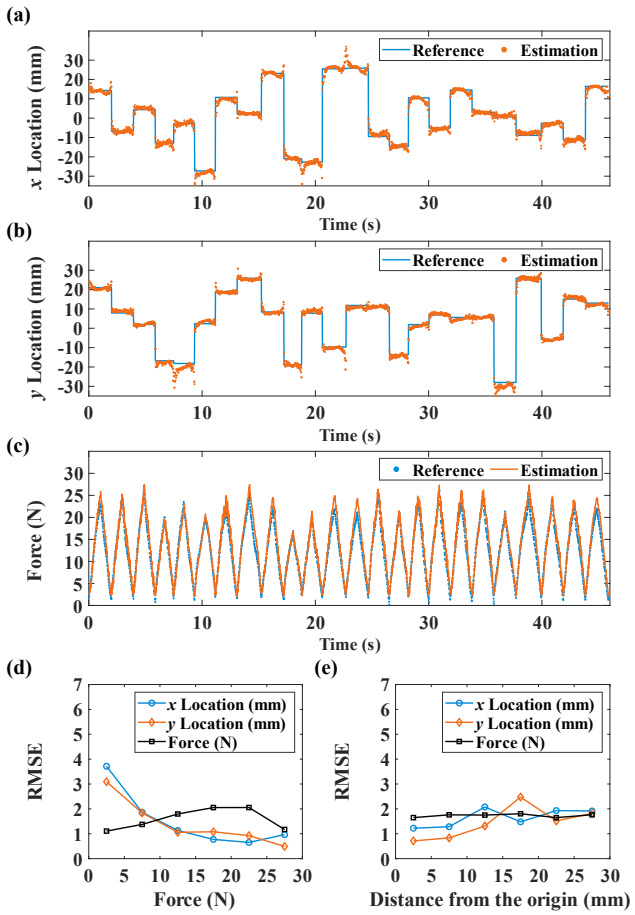

Fig. 12. Experimental results for the curved skin cover: the estimated locations of in (a) x- and (b) y-axis and (c) magnitudes of the applied forces and the RMSE values of the estimations with increments of (d) 5 N of force and (e) 5 mm of displacement. (This part shows various cases among the estimation results.) The RMSE values were evaluated using the test data acquired at random locations shown in Fig. 9(d). Force at each location was continuously increased up to the limit and decreased back to the initial.

and the angle at which it comes into contact with the skin can cause it to slide or rub against the surface. This can result in larger ranges of RMSE compared to cases where the skin surface is flat and the indenter makes contact perpendicular to it. The RMSE for estimating the locations every $5\,\mathrm{mm}$ from the origin is shown in Fig. 12(e). The result of hysteresis analysis is provided in APPENDIX E.

V. Application

We demonstrate two application areas where the proposed robotic skin can be effective on improving the performance: remote manipulation and autonomous control of robots. The application showcases the capacity to leverage tactile information from the skin to enable interaction with external environments, thereby enhancing the robot's environmental awareness and overall functionality. By enabling the robot to sense and respond to its surroundings, the skin facilitates improved control, dexterity, and potential for survival. In summary, the skin plays a critical role in the robot's ability to interact with and understand its environment, leading to increased performance and adaptability.

The skin modules were arranged at 60° intervals around a robotic arm to provide complete 360° coverage, with appropriate curvature and skin radius as illustrated in Fig. 4. In the demonstrated scenario, all contacts involved cylinder-to-cylinder interactions, resulting in ideal line forces. However, when encountering obstacles, surface contacts and forces may occur, leading to deformation. In such cases, each module estimates the magnitude of the net force and the location of the force area's centroid. (See Section III-D-3 for further details.)

A. Remote Robot Manipulation

The robotic skin was mounted on a robotic arm close to the end-effector, and the arm was controlled by a human operator using a haptic feedback device. The user was asked to move the robot by manipulating the haptic device. When the robot makes a contact with an unknown object, the information on the contact force was provided to the operator through the force feedback of the haptic device. The force feedback includes the magnitude and the direction, which is calculated

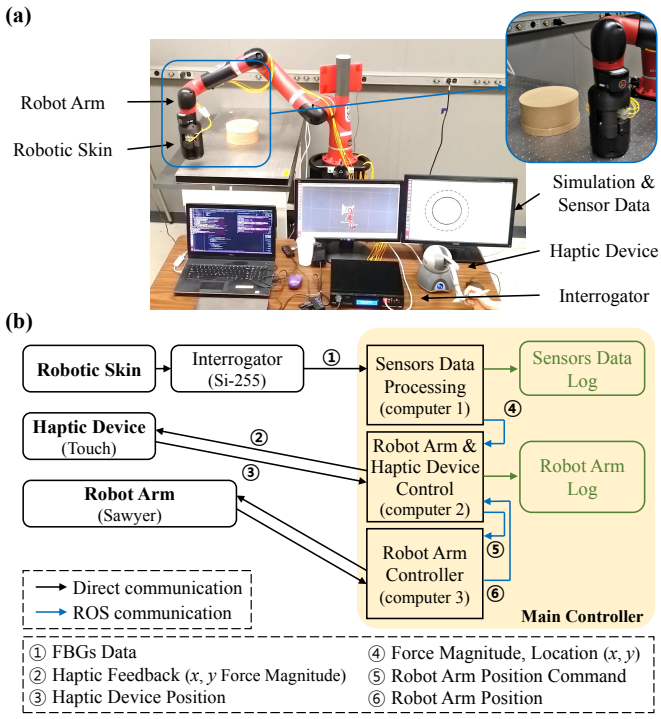

Fig. 13. (a) Robot arm and operator setup for shape tracing by remote robot manipulation. The robot arm, the haptic device, and the interrogator are, respectively, connected to each computer. (b) System configuration and data flow for shape tracing by remote robot manipulation.

by the force magnitude and location estimation of the robotic skin. We conducted two experiments in this demonstration: shape tracing of an unknown object and path finding with obstacle avoidance. During the experiments, force feedback was the only information provided to the operator in real time.

The entire system, comprising the robotic arm, haptic device, skin modules, and interrogator, was integrated and communicated data via the Robot Operating System (ROS)[1]. Specifically, communication with the skin modules was facilitated through LAN communication using the interrogator, and libraries were utilized to interface with the interrogator[2]. This software was then integrated with the main controller via ROS, which handled sensor data processing, robotic arm and haptic device control, real-time visualization, and logging modules. The controller also communicated with the haptic device and robotic arm using ROS.

In the sensor data processing stage, the tactile information from each skin module was converted to the base coordinate system to enable the representation of all information, including the robot arm and skin, in a unified space. The base coordinate was defined as the center of the cylinder formed by the skin. Additionally, the position and direction of external forces detected by each skin module were transformed with respect to the base coordinate system, leveraging homogeneous transformation matrices.

[1][Online]. https://www.ros.org/

[2][Online]. https://lunainc.com/product/hyperion-si255

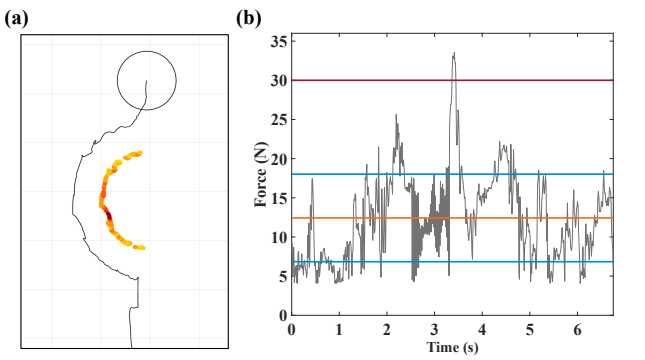

Fig. 14. Shape tracing results with a haptic device. (a) Position result. The black line is the robot arm path, and the black circle is current position of the robot arm. The yellow to red dots show the locations of the contacts, and the more red means the closer to the force limit (30 N). The criteria to set the force limit was discussed in Section IV-A. (b) Force response during the experiment. The red, orange and blue lines indicate the upper limit (30 N), the average, and range of the standard deviation of the measured force, respectively.

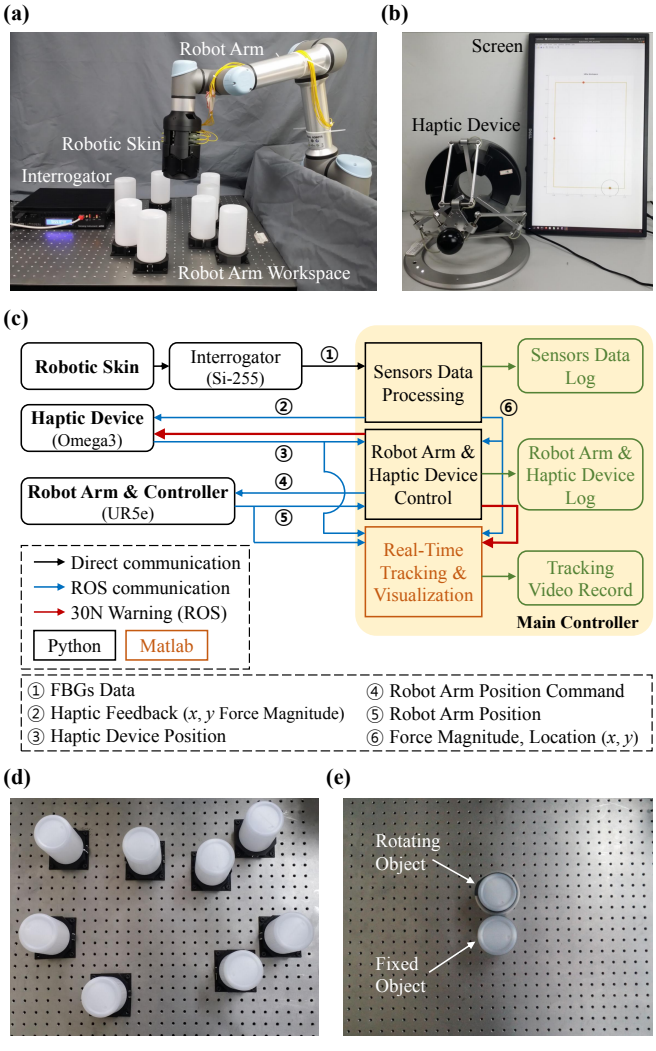

Fig. 15. (a) Robot arm setup. The robot arm and the interrogator are, respectively, connected to the computer using the LAN communication. (b) Operator setup. (c) System configuration and data flow. (d) Multi obstacles for path finding experiment with obstacle avoidance (Experimental setup). This setup was used in remote robot manipulation and in autonomous robot control. (e) Objects for object manipulation experiment through force control (Experimental setup). This setup was used in autonomous robot control.

1) Shape Tracing: The skin was mounted on a robotic arm (Sawyer, Rethink Robotics GmbH, Germany) that was controlled by a haptic device (Touch, 3D Systems, USA), as shown in Fig. 13. The operator was asked to start the experiment by moving the robot arm straight forward using the manipulator of the haptic device. As soon as the robot touches an object fixed on the ground, the operator feels the contact through force feedback. Then, the operator was asked to detour the object maintaining the contact. If the operator applies too large force to the object, it is hard to detour it. If the force is too small, it is easy to lose the contact. This task was possible, since the end of the arm was surrounded by the skin that can detect both the magnitude and the location of the contact force. The operator was able to maintain the contact during the experiment, as shown in Fig. 14. The average force applied to the object was $12.43\,\mathrm{N}$ with a standard deviation of $5.59\,\mathrm{N}$. As a result, the robotic skin allows the operator to recognize the shape of an unknown object and helps to interact safely with surroundings.

2) Path Finding with Obstacle Avoidance: The next experiment is extension of the previous one by increasing the number of the objects and the travel complexity of the robot. The skin was mounted on an industrial robot arm (UR5e, Universal Robots, Denmark) that was controlled by a haptic device (Omega3, Force Dimension, Switzerland), as shown in Fig. 15. In this experiment, the operator was asked to move the robot to two waypoints one after the other and to return to the starting location. Before starting the experiment, the operator has information only on the initial position of the robot and the locations of the two waypoints on a map (Fig. 16(a)). As soon as the robot moves, the trajectory of the robot and the contact information of the obstacles up to the current position are provided on the screen. The operator feels the contact force during the experiment through the force feedback of the haptic device. If the contact force is greater than the threshold, the robot arm returns to its 1.3 seconds previous position and the haptic device also returns to the origin. The operator was able to complete the task even with multiple obstacles using the contact information provided by the skin, as shown in Fig. 16. The average force applied to the obstacles during the experiment was $9.23\,\mathrm{N}$ with a standard deviation of $4.35\,\mathrm{N}$. Therefore, the robotic skin is able to help in exploring the surroundings and creating trajectory by providing the location of objects. The robotic skin also enables the operator to protect the robot from the excessive contact force.

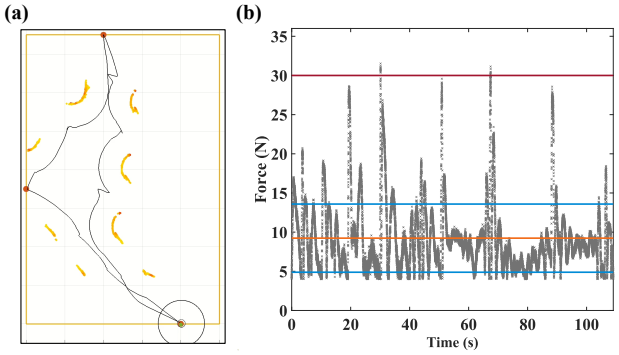

Fig. 16. Path finding results with obstacle avoidance by remote robot manipulation. (a) Position result. The large brown dots are target points. Other expressions are the same as Fig. 14(a). (b) Force result when the forces are applied the robotic skin. The expression method is the same as Fig. 14(b).

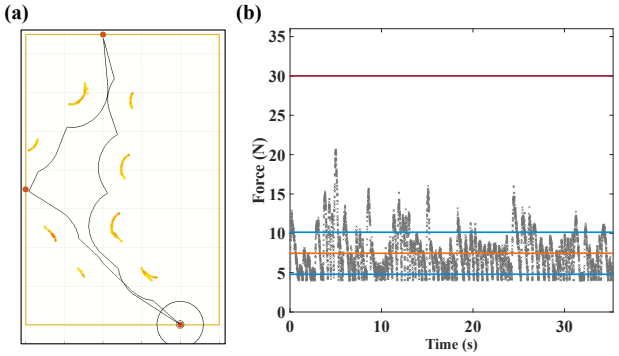

Fig. 17. Path finding results with obstacle avoidance by autonomous robot control. (a) Position result. The large brown dots are target points. Other expressions are the same as Fig. 14(a). (b) Force result when the forces are applied the robotic skin. The expression method is the same as Fig. 14(b).

B. Autonomous Robot Control

We demonstrate the performance of autonomous robot control using the proposed skin system. We conducted two experiments: path finding with obstacle avoidance and manipulation of a free-moving object through force control.

1) Path Finding with Obstacle Avoidance: The second experiment in section V-A was conducted with a human operator. However, in this experiment, the robot operated autonomously without an operator. The robot traveled passing two waypoints and returned to the starting point avoiding obstacles autonomously. The initial path of the robot was given only by straight lines that connect the origin and the waypoints. However, if the robot meets obstacles, it autonomously avoids them based on the estimated contact position while trying to keep the original trajectory as much as possible. The robot was successfully complete the task, as shown in Fig. 17. The average force applied to the obstacles during the experiment was $7.46\,\mathrm{N}$ with a standard deviation of $2.67\,\mathrm{N}$.

2) Object Manipulation through Force Control: Manipulation of a free-moving object requires a combination of detection of the contact location and sensing of the contact force of the target object, which can be enabled by our robotic skin. In this experiment, two same-sized cylindrical objects were prepared, as shown in Fig. 15(e). One was fixed on the ground and the other object can move freely around the first object. In this task, the robot was ordered to rotate the second cylinder around the first one while maintaining the contact and controlling the contact force. The trajectory was determined as shown in Fig. 18 [25], [26]. The direction of $\vec{v}_v$ is perpendicular to the direction of the external force from the center of the robotic skin, and the direction of $\vec{v}_h$ is opposite to the direction of the external force from the center of the robotic skin. The magnitude of $\vec{v}_h$ is proportional to that

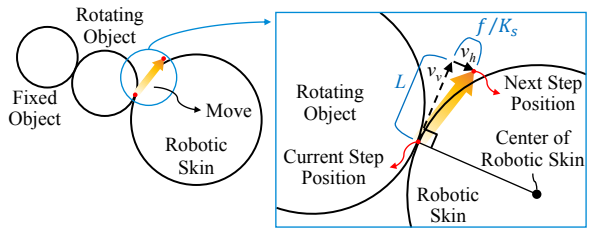

Fig. 18. Trajectory for obstacle avoidance.

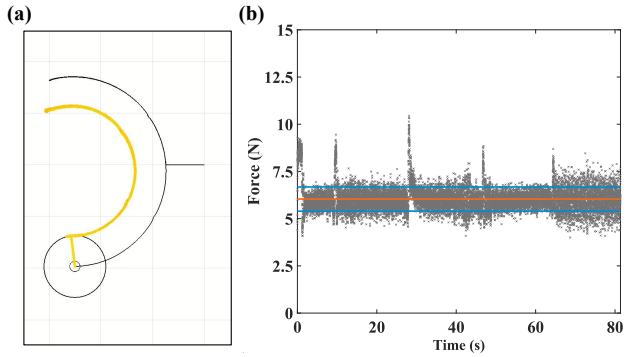

Fig. 19. Object manipulation results through force control by autonomous robot control. (a) Position result. The expression method is the same as Fig. 14(a). (b) Force result when the forces are applied the robotic skin. The expression method is the same as Fig. 14(b).

of the external force. (The detail control method is seen in Appendix C.) The contact location on the robot continuously changes during rotation, but a constant contact force needs to be applied even with the continuous change of the contact location.

During the experiment, the robot rotated the free-moving cylinder around the fixed one counterclockwise first and returned it to the original location by rotating it clockwise. The target force is $6\,\mathrm{N}$, and the result is shown as Fig. 19. The average force applied to the object was $6.04\,\mathrm{N}$ with an RMSE of $0.64\,\mathrm{N}$. The robotic skin allowed the robot to control the contact force on the surface of the arm autonomously even with the change of the position.

VI. Discussion

This paper introduces a modular robotic skin sensorized with FBGs and presents an associated model. The robotic skin serves to provide essential environmental information and facilitate interactions with objects during remote and autonomous robot operations. This enhanced functionality contributes to improved controllability, dexterity, and safety, as demonstrated in our applications. These improvements may also save the cost by increasing the likelihood of task success and reducing the occurrence of task failures or malfunctions.

The primary contribution of this research lies in the modular design of the optically sensorized robotic skin, which not only detects the location of contact but also measures the applied force. Each skin module of the robotic skin offers three DoFs, allowing the estimation of contact locations along the x and y axes, as well as the magnitude of the contact force. The modular design enhances the adaptability of the skin system, making it easily reconfigurable and scalable to suit different host structures.

Another contribution is the real-time processing of sensor data. We developed models based on force and moment equilibriums, incorporating geometric constraints, and optimized only for specific constant values where errors are anticipated. As only the modeling and optimized constants are used for sensor data processing, the processing speed is considerably fast, which enables real-time sensor data processing across multiple modules for various robotic situations. (Additional details on scalability are provided in APPENDIX D.)

The robotic skin demonstrates promise but exhibits potential areas for improvement, particularly in addressing estimation errors within the skin modules. When external forces disappear, the joint layer is expected to return to its initial position, owing to the elasticity of the wave springs in the S-L joints and beams. However, the presence of friction between the bead and bolt of the S-L joint, as well as between the bead and socket in the joint layer, impedes the complete restoration of the layer to its initial state. Although efforts have been made to mitigate friction by applying lubrication to the bead, socket, and bolt surfaces, the estimation accuracy remains suboptimal, especially in low force scenarios. This is due to the challenges associated with restoring the initial position after receiving low forces. A potential avenue for future research involves minimizing the impact of friction by designing the sensing structure as a single body with three degrees of freedom. Alternatively, more advanced machine learning techniques could be used to train the model on nonlinear effects, such as friction between components or the viscoelastic properties of polymer materials. This could lead to improved estimation results. (Additional details regarding characterization results using a basic machine learning model can be found in APPENDIX F.)

In prior studies, which employed hall effect and piezoresistive sensors, estimations were achieved with RMSEs ranging from 0.05 to $0.16\,\mathrm{N}$ for force estimation and ranging from 0.38-$0.98\,\mathrm{mm}$ for location estimation [32]. To further improve the sensing performance of our proposed mechanism, advanced machine learning techniques can be harnessed, and modifications to the dimensions and materials can be considered. For instance, employing a softer material for the sensing layer and thinner beams could result in larger strain for the same applied force, thereby reducing RMSEs in force perception by the robotic skin.

It is reasonable to use softer and lighter materials. The use of soft components within the sensor layer facilitates sufficient shifts in the peak wavelength of the FBGs even when subjected to lower forces. This leads to an enhanced minimum detectable force and accuracy. Although the use of soft materials induces challenges, such as hysteresis and durability concerns, these issues can be effectively addressed by advanced machine learning techniques and design optimization. Moreover, reduction in weight of the skin module could be achieved by fabricating the layer and the cover components using lightweight polymer materials, considering that the weight of the optical fiber with FBGs

is negligible. When the weight is reduced, it is possible to minimize the constraints imposed on a robot's payload and its dynamic characteristics even when a substantial number of sensor modules are installed to the robot.

An additional improvement to the current design involves estimating the direction of the contact force by adding additional DoFs. This allows the robotic skin to detect shear forces as well as normal forces, opening up possibilities for more sophisticated manipulation in robotic applications. To understand the impact of shear force, it is important to conduct a thorough analysis of estimation results and accuracy when forces are applied to surfaces of varying sizes and curvatures, emanating from diverse angles.

VII. Conclusion

In this study, we successfully developed a versatile and robust robotic skin with a modular structure. This skin detect both the magnitude and location of contact forces, using the embedded FBG strain sensors. This sensing technology not only delivers highly accurate and precise force measurements but also exhibits immunity to electromagnetic noise, making it ideal for use in harsh environments, including EMI and radioactive conditions.

Our application experiments demonstrate the performance of the robotic skin for remote manipulation and autonomous control of robots, highlighting its potential for a wide range of real-world applications in various fields, such as healthcare, manufacturing, and space exploration. Overall, our findings indicate that the proposed robotic skin has the potential to significantly improve the safety, efficiency, and autonomy of robotic systems, allowing for the development of more advanced and sophisticated robotic technologies in the future.

Appendix I
Beam Deflection

Fig. 5 shows constants, variables, and conditions for the beam location estimation. The force, F, is applied to the tip of the beam, and the beam surface at $x_1 = 0$ is fixed. The length constrains are always satisfied as follows

$$x_1 + x_2 = l_1 + l_2 = L. \tag{19}$$

The width is given as Eqn. (6). When x_1 is larger than 0 and smaller than l_1, the moment of inertia (I_1) and moment (M_1) are expressed as Eqn. (9). The second derivative of v_1 is as follows [67]

$$\frac{d^2v_1}{dx_1^2} = \frac{M_1}{EI_1} = \frac{12L}{Ewh^3}F, \tag{20}$$

which serves as the initial point for deriving the deflection through the process of integration. This equation can be integrated for x_1, and applied the boundary condition at $x_1 = 0$ as follows

$$\begin{aligned} \frac{dv_1}{dx_1} =& \frac{12L}{Ewh^3}Fx_1 + C_1 = \frac{12L}{Ewh^3}Fx_1, \\ & \left(\because dv_1/dx_1|_{x_1=0} = 0\right) \\ v_1 =& \frac{6L}{Ewh^3}Fx_1^2 + C_2 = \frac{6L}{Ewh^3}Fx_1^2. \\ & \left(\because v_1|_{x_1=0} = 0\right) \end{aligned} \tag{21}$$

Thus, $\frac{dv_1}{dx_1}$ and v_1 at $x_1 = l_1$ are given as

$$\begin{aligned} \left.\frac{dv_1}{dx_1}\right|_{x_1=l_1} =& \frac{12L}{Ewh^3}Fl_1 = \frac{V_1}{E}F, \\ v_1|_{x_1=l_1} =& \frac{6L}{Ewh^3}Fl_1^2 = \frac{V_2}{E}F \end{aligned} \tag{22}$$

where V_1 and V_2 are constants of l_1, L, w, and h.

When x_2 is larger than 0 and smaller than l_2, the moment of inertia (I_2) and moment (M_2) are expressed as Eqn. (9). The second derivative of v_2 is as follows

$$\frac{d^2v_2}{dx_2^2} = \frac{M_2}{EI_2} = -\frac{12l_2x_2}{h^3((m-n)x_2 + nl_2)}\frac{F}{E} = -\frac{f''(x_2)}{E}F \tag{23}$$

where $f''(x_2)$ is function of l_2, h, m, n, and x_2.

$x_1 = l_1$ is equal location to $x_2 = l_2$. Consequently, Eqn. (23) can be integrated for x_2, and applies the boundary condition at $x_2 = l_2$ as follows

$$\begin{aligned} \frac{dv_2}{dx_2} =& -\frac{f'(x_2)}{E}F + C_3 = \left(-f'(x_2) + f'(l_2) + V_1\right)\frac{F}{E}, \\ & \left(\because dv_2/dx_2|_{x_2=l_2} = dv_1/dx_1|_{x_1=l_1}\right) \\ v_2 =& \left(-f(x_2) + f'(l_2)x_2 + V_1x_2\right)\frac{F}{E} + C_4 \\ =& \left[-f(x_2) + (f'(l_2) + V_1)(x_2 - l_2) + f(l_2) + V_2\right]\frac{F}{E}. \\ & \left(\because v_2|_{x_2=l_2} = v_1|_{x_1=l_1}\right) \end{aligned} \tag{24}$$

If we apply $x_2 = 0$, we can get the deflection at the tip as follows

$$\begin{aligned} v_2|_{x_2=0} =& \left[-f(0) - (f'(l_2) + V_1)l_2 + f(l_2) + V_2\right]\frac{F}{E} \\ =& K_vF \end{aligned} \tag{25}$$

where K_v is the deflection proportional constant. Since the deflection at $x_2 = 0$ is proportional to F, the location of the beam forces can be determined by the magnitude of the force. This linearity is also verified by the FEA as shown in Fig. 6(c).

Appendix II
Specifications of FBGs and Interrogator

Each FBG has a resolution in strain measurement of up to 8×10^{-3} strain. In order to enable the simultaneous measurement of a greater number of sensors with a single interrogator, we adjusted the wavelength bands to limit the measurement range to 5×10^{-3} strain. Consequently, each FBG is able to measure up to 5×10^{-3} strain. Each FBG has a sensing length of $3\,\mathrm{mm}$, and the optical fiber has a polyimide coating with low optical loss in bending, which

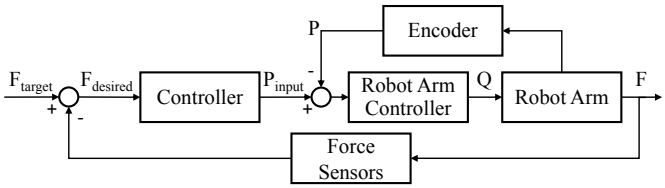

Fig. 20. Position-based force-control block diagram. F_{target} is the target contact force and F is the contact force. P_{input}, $P_{desired}$, and P are, respectively, the input command end-effector position, the desired end-effector position, and the end-effector position. Q is the input commands of each joint.

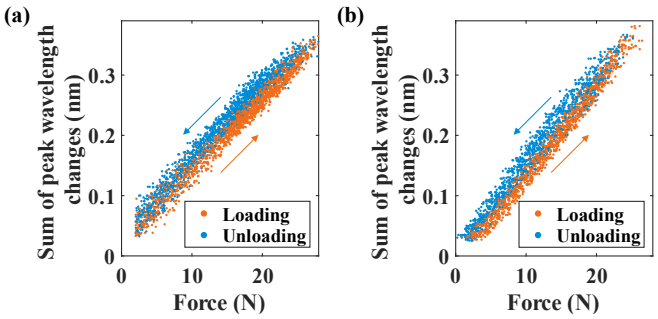

Fig. 21. Results of hysteresis analysis for the skin module with (a) a flat skin cover and (b) a curved skin cover.

improves robustness in sensing when attaching an optical fiber with a small radius of curvature to a small skin module.

The interrogator has 16 channels, and is capable of detecting a range of $100\,\mathrm{nm}$ in each channel. Given that each FBG needs a wavelength spacing of $5\,\mathrm{nm}$ to measure up to 5×10^{-3} strain, the proposed system with one interrogator can concurrently estimate up to 80 modules. These modules can cover the area of a square with a side length of $4.83\,\mathrm{m}$. The device receives reflected lights from all the channels at $1000\,\mathrm{Hz}$ and detects peak wavelengths through post-processing. We tested the interrogator's noise level and found it to be around 1.2×10^{-2} nm, corresponding to a strain sensitivity of 1.2×10^{-5} for the FBG.

Appendix III
Control Method

To control the contact force, a mass-spring model was used for the force control [68], which is expressed with

$$m\ddot{x} + K_s x = f_c \tag{26}$$

where m is the mass of the robotic skin arm, K_s is the effective stiffness of the skin and environment, and f_c represents the control force by the robot arm. When we assume the object is static, the measured contact force (f_s) at the skin is given as

$$f_s = K_s x. \tag{27}$$

The contact force is controlled by a proportional-integral-derivative (PID) controller [68], [69] as

$$f_c = f_s - m\left[K_d \dot{f}_s + K_p\left(f_s - f_d\right) + K_i \int \left(f_s - f_d\right) dt\right] \tag{28}$$

where K_d, K_p, and K_i are the derivative, proportional, and integral gains, respectively, and f_d is desired force. Furthermore, the closed loop behavior can be expressed with the above equations as

$$\ddot{x} + \left[K_d \dot{f}_s + K_p\left(f_s - f_d\right) + K_i \int \left(f_s - f_d\right)\right] = 0. \tag{29}$$

Since the arm is controlled by the position command, the control force is converted to the control position based on Eqn. (27). The next control position in the horizontal direction of the control force is thus $x_{c_h} = f_c/K_s$. Also, to rotate around the fixed object, the next control position in the perpendicular direction of the control force is $x_{c_p} = L$ (Fig. 18). The estimated force obtained through the robotic skin is used for computing the force errors, and these values serve as the inputs to the controller, as shown in Fig. 20.

Appendix IV
Scalability and Force Sensing Range

The skin module can be designed with various sizes, curvatures, and ranges of detectable forces. For a smaller module, a section of at least 3 mm for FBG attachment should be secured on the beam covered by a composite skin layer made by precision machining. When fabricating a larger module, the beam should not undergo plastic deformation even with the maximum force applied. The prestress should be also adjusted to maintain the contact between the beam and the joint.

The minimum and the maximum detectable forces are design parameters that can be adjusted. In this paper, we selected those forces by considering the force range required to implement the proposed application and the size of the robot arm where the skin will be mounted. Specifically, we considered the positional accuracy and the speed of the robot arm, the stiffness of the obstacles, and the control performance of the robot arm in the case of remote operation. However, the skin's performance can be enhanced by altering the materials and dimensions of the beam layer in each skin module or by utilizing a more high-performance interrogator.

Appendix V
Hysteresis Analysis

Fig. 21 shows the results of hysteresis analysis in both cases of a flat and a curved skin cover.

Appendix VI
Characterization by Machine Learning

We developed a Pytorch[3]-based deep neural network (DNN) model with an input layer of three nodes, followed by three hidden layers (256, 128, and 64 nodes), and an output layer with three nodes. The DNN model was optimized using Adam optimizer with a learning rate of 0.001 and trained for 1000 epochs with a batch size of 256. We evaluated the model's performance using the test data, as shown in Fig. 22

[3][Online]. https://pytorch.org/

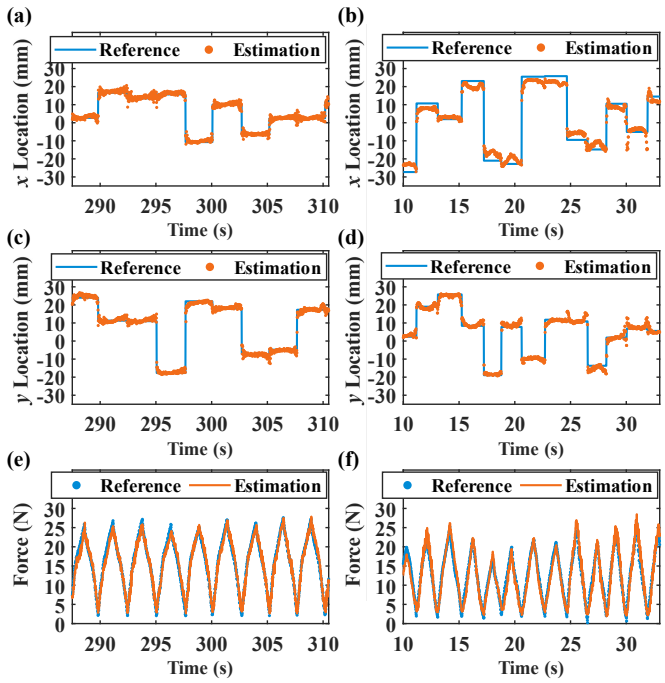

Fig. 22. Estimation results using machine learning (a, e, and e) for a flat skin cover and (b, d, and f) for a curved skin cover. The data used here are the same as those of Figs. 11 and 12. The plots show the estimation results for (a and b) x and (c and d) y locations and (e and f) the magnitude of the applied force.

and summarized in Table I. The estimated results align match those obtained in Section IV.

The skin module with the flat cover outperformed the DNN model, but for the curved cover, the DNN model showed better force estimation but less accurate location estimation due to the non-linear effects from the skin curvature and friction. Advanced machine learning techniques may improve the accuracy by capturing these effects.

REFERENCES

[1] M. Spenko, S. Buerger, and K. Iagnemma, *The DARPA Robotics Challenge Finals: Humanoid Robots To The Rescue*. Cham, Switzerland: Springer International Publishing, 2018.

[2] L. Penco, N. Scianca, V. Modugno, L. Lanari, G. Oriolo, and S. Ivaldi, "A multimode teleoperation framework for humanoid loco-manipulation: An application for the iCub robot," *IEEE Robot. Autom. Mag.*, vol. 26, no. 4, pp. 73–82, 2019.

[3] C. Wong, E. Yang, X. Yan, and D. Gu, "An overview of robotics and autonomous systems for harsh environments," in *Proc. Int. Conf. Autom. Comput. (ICAC)*, 2017, pp. 1–6.

[4] N. Marturi, A. Rastegarpanah, C. Takahashi, M. Adjigble, R. Stolkin, S. Zurek, M. Kopicki, M. Talha, J. A. Kuo, and Y. Bekiroglu, "Towards advanced robotic manipulation for nuclear decommissioning: A pilot study on tele-operation and autonomy," in *Proc. Int. Conf. Robot. Autom. Humanitarian Appl. (RAHA)*, 2016, pp. 1–8.

TABLE I

ESTIMATION RESULTS USING MACHINE LEARNING (DNN) AND MODELING

RMSE	Flat skin cover		Curved Skin Cover	
	DNN	Modeling	DNN	Modeling
x location (mm)	1.53	1.85	3.08	1.80
y location (mm)	1.54	1.91	2.01	1.67
Force magnitude (N)	1.25	1.45	1.66	1.74

[5] J. Ramos, A. Wang, and S. Kim, "Robot-human balance state transfer during full-body humanoid teleoperation using divergent component of motion dynamics," in *Prof. IEEE Int. Conf. Robot. Autom. (ICRA)*, 2016, pp. 1587–1592.

[6] F. Abi-Farrajl, B. Henze, A. Werner, M. Panzirsch, C. Ott, and M. A. Roa, "Humanoid teleoperation using task-relevant haptic feedback," in *Proc. IEEE/RSJ Int. Conf. Intell. Robot. Syst. (IROS)*, 2018, pp. 5010–5017.

[7] J. Kofman, X. Wu, T. Luu, and S. Verma, "Teleoperation of a robot manipulator using a vision-based human-robot interface," *IEEE Trans. Ind. Electron.*, vol. 52, no. 5, pp. 1206–1219, 2005.

[8] Y.-L. Park, S. C. Ryu, R. J. Black, K. K. Chau, B. Moslehi, and M. R. Cutkosky, "Exoskeletal force sensing end-effectors with embedded optical fiber Bragg grating sensors," *IEEE Trans. Robot.*, vol. 25, no. 6, pp. 1319–1331, 2009.

[9] C. Fox, M. Evans, M. Pearson, and T. Prescott, "Tactile SLAM with a biomimetic whiskered robot," in *Proc. IEEE Int. Conf. Robot. Autom. (ICRA)*, 2012, pp. 4925–4930.

[10] Q. K. Luu, N. H. Nguyen, and V. A. Ho, "Simulation, learning, and application of vision-based tactile sensing at large scale," *IEEE Trans. Robot.*, vol. 6, no. 3, pp. 4361–4368, 2023.

[11] F. Mazzini and S. Dubowsky, "An experimental validation of robotic tactile mapping in harsh environments such as deep sea oil well sites," in *Experimental Robotics*, O. Khatib, V. Kumar, and G. Sukhatme, Eds. Berlin/Heidelberg, Germany: Springer, 2014, vol. 79, pp. 557–570.

[12] R. S. Dahiya, G. Metta, M. Valle, and G. Sandini, "Tactile sensing—from humans to humanoids," *IEEE Trans. Robot.*, vol. 26, no. 1, pp. 1–20, 2010.

[13] A. Schmitz, P. Maiolino, M. Maggiali, L. Natale, G. Cannata, and G. Metta, "Methods and technologies for the implementation of large-scale robot tactile sensors," *IEEE Trans. Robot.*, vol. 27, no. 3, pp. 389–400, 2011.

[14] P. Mittendorfer and G. Cheng, "Humanoid multimodal tactile-sensing modules," *IEEE Trans. Robot.*, vol. 27, no. 3, pp. 401–410, 2011.

[15] Y.-L. Park, B.-r. Chen, and R. J. Wood, "Design and fabrication of soft artificial skin using embedded microchannels and liquid conductors," *IEEE Sens. J.*, vol. 12, no. 8, pp. 2711–2718, 2012.

[16] B. Zhang, J. Wang, G. Q. Zhang, S. Choi, R. Boca, T. A. Fuhlbrigge, and T. Groth, "Teleoperation of machines having at least one actuated mechanism and a fault detection and recovery system," U.S. Patent 9 682 480, jun. 20, 2017.

[17] S. J. Yoon, M. Choi, B. Jeong, and Y.-L. Park, "Elongatable gripper fingers with integrated stretchable tactile sensors for underactuated grasping and dexterous manipulation," *IEEE Trans. Robot.*, vol. 38, no. 4, pp. 2179–2193, 2022.

[18] P. Nadeau, M. Abbott, D. Melville, and H. S. Stuart, "Tactile sensing based on fingertip suction flow for submerged dexterous manipulation," in *Proc. IEEE Int. Conf. Robot. Autom. (ICRA)*, 2020, pp. 3701–3707.

[19] J. Jung, M. Park, D. Kim, and Y.-L. Park, "Optically sensorized elastomer air chamber for proprioceptive sensing of soft pneumatic actuator," *IEEE Robot. Autom. Lett.*, vol. 5, no. 2, pp. 2333–2340, 2020.

[20] J. I. Kim, D. Kim, M. Krebs, Y. S. Park, and Y.-L. Park, "Force sensitive robotic end-effector using embedded fiber optics and deep learning characterization for dexterous remote manipulation," *IEEE Robot. Autom. Lett.*, vol. 4, no. 4, pp. 3481–3488, 2019.

[21] J. P. Clark, G. Lentini, F. Barontini, M. G. Catalano, M. Bianchi, and M. K. O'Malley, "On the role of wearable haptics for force feedback in teleimpedance control for dual-arm robotic teleoperation," in *Proc. IEEE Int. Conf. Robot. Autom. (ICRA)*, 2019, pp. 5187–5193.

[22] E. Aranda-Michel, J. Yi, J. Wirekoh, N. Kumar, C. N. Riviere, D. S. Schwartzman, and Y.-L. Park, "Miniaturized robotic end-effector with piezoelectric actuation and fiber optic sensing for minimally invasive cardiac procedures," *IEEE Sens. J.*, vol. 18, no. 12, pp. 4961–4968, 2018.

[23] V. J. Lumelsky and E. Cheung, "Real-time collision avoidance in teleoperated whole-sensitive robot arm manipulators," *IEEE Trans. Syst., Man Cybern.*, vol. 23, no. 1, pp. 194–203, 1993.

[24] G. Shin, S. Lee, and Y.-L. Park, "Selective patterning of conductive elastomers embedded with silver powders and carbon nanotubes for stretchable electronics," *IEEE Robot. Autom. Lett.*, vol. 7, no. 2, pp. 4983–4990, 2022.

[25] N. F. Lepora, K. Aquilina, and L. Cramphorn, "Exploratory tactile servoing with active touch," *IEEE Robot. Autom. Lett.*, vol. 2, no. 2, pp. 1156–1163, 2017.

[26] U. Martinez-Hernandez, T. J. Dodd, M. H. Evans, T. J. Prescott, and N. F. Lepora, "Active sensorimotor control for tactile exploration," *Robot. Auton. Syst.*, vol. 87, pp. 15–27, 2017.

[27] V. Pruks, K. Lee, and J. Ryu, "Shared teleoperation for nuclear plant robotics using interactive virtual guidance generation and shared autonomy approaches," in *Pro. Int. Conf. Ubiquitous Robot. (UR)*, 2018, pp. 91–95.

[28] D. Hughes, J. Lammie, and N. Correll, "A robotic skin for collision avoidance and affective touch recognition," *IEEE Robot. Autom. Lett.*, vol. 3, no. 3, pp. 1386–1393, 2018.

[29] L. Jiang, K. Low, J. Costa, R. J. Black, and Y.-L. Park, "Fiber optically sensorized multi-fingered robotic hand," in *Proc. IEEE/RSJ Int. Conf. Intell. Robot. Syst. (IROS)*, 2015, pp. 1763–1768.

[30] T. Kim, J. Park, S. J. Yoon, D. H. Kong, H.-W. Park, and Y.-L. Park, "Design of a lightweight inflatable sensing sleeve for increased adaptability and safety of legged robots," in *Proc. IEEE Int. Conf. Soft Robot. (RoboSoft)*, 2019, pp. 257–264.

[31] Y. Pang, X. Xu, S. Chen, Y. Fang, X. Shi, Y. Deng, Z.-L. Wang, and C. Cao, "Skin-inspired textile-based tactile sensors enable multifunctional sensing of wearables and soft robots," *Nano Energy*, vol. 96, p. 107137, 2022.

[32] Z. Lu, X. Gao, and H. Yu, "GTac: A biomimetic tactile sensor with skin-like heterogeneous force feedback for robots," *IEEE Sens. J.*, vol. 22, no. 14, pp. 14 491–14 500, 2022.

[33] Y. Yan, Z. Hu, Z. Yang, W. Yuan, C. Song, J. Pan, and Y. Shen, "Soft magnetic skin for super-resolution tactile sensing with force self-decoupling," *Sci. Robot.*, vol. 6, no. 51, p. eabc8801, 2021.

[34] I. H. Taylor, S. Dong, and A. Rodriguez, "Gelslim 3.0: High-resolution measurement of shape, force and slip in a compact tactile-sensing finger," in *Proc. Int Conf. Robot. Autom. (ICRA)*, 2022, pp. 10 781–10 787.

[35] A. C. Abad and A. Ranasinghe, "Visuotactile sensors with emphasis on gelsight sensor: A review," *IEEE Sens. J.*, vol. 20, no. 14, pp. 7628–7638, 2020.

[36] A. Albini and G. Cantana, "Pressure distribution classification and segmentation of human hands in contact with the robot body," *Int. J. Robot. Res.*, vol. 39, no. 6, pp. 641–752, 2020.

[37] L. V. Duong and V. A. Ho, "Large-scale vision-based tactile sensing for robot links: Design, modeling, and evaluation," *IEEE Trans. Robot.*, vol. 37, no. 2, pp. 390–403, 2021.

[38] X. Duan, S. Taurand, and M. Soleimani, "Artificial skin through super-sensing method and electrical impedance data from conductive fabric with aid of deep learning," *Sci. Rep.*, vol. 9, no. 1, p. 8831, 2019.

[39] H. Park, H. Lee, K. Park, S. Mo, and J. Kim, "Deep neural network approach in electrical impedance tomography-based real-time soft tactile sensor," in *Proc. IEEE/RSJ Int. Conf. Intell. Robot. Syst. (IROS)*, 2019, pp. 7447–7452.

[40] Y. Zhang, J. Yang, X. Hou, G. Li, L. Wang, N. Bai, M. Cai, L. Zhao, Y. Wang, J. Zhang, K. Chen, X. Wu, C. Yang, Y. Dai, Z. Zhang, and C. F. Guo, "Highly stable flexible pressure sensors with a quasi-homogeneous composition and interlinked interfaces," *Nat. Commun.*, vol. 13, p. 1317, 2022.

[41] S. R. A. Ruth, L. Beker, H. Tran, V. R. Feig, N. Matsuhisa, and Z. Bao, "Rational design of capacitive pressure sensors based on pyramidal microstructures for specialized monitoring of biosignals," *Adv. Funct. Mater.*, vol. 30, no. 29, p. 1903100, 2020.

[42] L. Massari, G. Fransvea, M. F. Jessica D'Abbraccio, G. Terruso, A. Aliperta, G. D'Alesio, M. Zaltieri, E. Schena, E. Palermo, E. Sinibaldi, and C. M. Oddo, "Functional mimicry of ruffini receptors with fibre bragg gratings and deep neural networks enables a bio-inspired large-area tactile-sensitive skin," *Nat. Mach. Intell.*, vol. 4, no. 5, pp. 425–435, 2022.

[43] L. Massari, E. Schena, C. Massaroni, P. Saccomandi, A. Menciassi, E. Sinibaldi, and C. M. Oddo, "A machine-learning-based approach to solve both contact location and force in soft material tactile sensors," *Soft Robot.*, vol. 7, no. 4, pp. 409–420, 2020.

[44] T. L. T. Lun, K. Wang, J. D. L. Ho, K.-H. Lee, K. Y. Sze, and K.-W. Kwok, "Real-time surface shape sensing for soft and flexible structures using fiber bragg gratings," *IEEE Robot. Autom. Lett.*, vol. 4, no. 2, pp. 1454–1461, 2019.

[45] K. O. Hill and G. Meltz, "Fiber Bragg grating technology fundamentals and overview," *J. Lightwave Technol.*, vol. 15, no. 8, pp. 1263–1276, 1997.

[46] A. D. Kersey, M. A. Davis, H. J. Patrick, M. LeBlanc, K. P. Koo, C. G. Askins, M. A. Putnam, and E. J. Friebele, "Fiber grating sensors," *J. Lightwave Technol.*, vol. 15, no. 8, pp. 1442–1463, 1997.

[47] S. Lee, "Modularized robotic skin sensorized by fiber optic force sensing for remote and autonomous robot operation," M.S. Thesis, Seoul National University, Seoul, Republic of Korea, 2021.

[48] J.-S. Heo, J.-H. Chung, and J.-J. Lee, "Tactile sensor arrays using fiber Bragg grating sensors," *Sens. Actuators, A*, vol. 126, no. 2, pp. 312–327, 2006.

[49] W. Zhou, X. Dong, K. Ni, C. Chan, and P. Shum, "Temperature-insensitive accelerometer based on a strain-chirped FBG," *Sens. Actuators, A*, vol. 157, no. 1, pp. 15–18, 2017.

[50] A. Mohammed and S. Djurović, "FBG thermal sensing features for hot spot monitoring in random wound electric machine coils," *IEEE Sens. J.*, vol. 17, no. 10, pp. 3058–3067, 2017.

[51] Y.-L. Park, S. Elayaperumal, B. Daniel, S. C. Ryu, M. Shin, J. Savall, R. J. Black, B. Moslehi, and M. R. Cutkosky, "Real-time estimation of 3-D needle shape and deflection for mri-guided interventions," *IEEE/ASME Trans. Mechatron.*, vol. 15, no. 6, pp. 906–915, 2010.

[52] J. Song, Q. Jiang, Y. Huang, Y. Li, Y. Jia, X. Rong, R. Song, and H. Liu, "Research on pressure tactile sensing technology based on fiber bragg grating array," *Photonic Sens.*, vol. 5, no. 3, pp. 263–272, 2015.

[53] R. J. Roesthuis and S. Misra, "Steering of multisegment continuum manipulators using rigid-link modeling and fbg-based shape sensing," *IEEE Trans. Robot.*, vol. 23, no. 2, pp. 372–382, 2016.

[54] S. Sareh, Y. Noh, M. Li, T. Ranzani, H. Liu1, and K. Althoefer, "Macrobend optical sensing for pose measurement in soft robot arms," *Smart Mater. Struct.*, vol. 24, no. 12, p. 125024, 2015.

[55] Z. Dong, X. Wang, G. Feng, Z. He, J. D.-L. Ho, C.-L. Cheung, W. L. Tang, X. Xie, L. Liang, H.-C. Chang, C. K. Ching, and K.-W. Kwok, "Shape tracking and feedback control of cardiac catheter using MRI-guided robotic platform–validation with pulmonary vein isolation simulator in MRI," *IEEE Trans. Robot.*, 2022.

[56] K. Sun, M. Li, S. Wang, G. Zhang, H. Liu, and C. Shi, "Development of a fiber bragg grating-enabled clamping force sensor integrated on a grasper for laparoscopic surgery," *IEEE Sens. J.*, vol. 21, no. 15, pp. 16 681–16 690, 2021.

[57] W. W. Morey, J. R. Dunphy, and G. Meltz, "Multiplexing fiber Bragg grating sensors," *Fiber Integr. Opt.*, vol. 10, no. 4, pp. 351–360, 1991.

[58] A. D. Kersey, T. A. Berkoff, and W. W. Morey, "Multiplexed fiber Bragg grating strain-sensor system with a fiber Fabry-Perot wavelength filter," *Opt. Lett.*, vol. 18, no. 16, pp. 1370–1372, 1993.

[59] P. K. C. Chan, W. Jin, and M. Suleyman Demokan, "FMCW multiplexing of fiber bragg grating sensors," *IEEE J. Sel. Top. Quantum Electron.*, vol. 6, no. 5, pp. 756–763, 2000.

[60] J. Hu, Z. Chen, and C. Yu, "150-km long distance FBG temperature and vibration sensor system based on stimulated Raman amplification," *J. Lightwave Technol.*, vol. 30, no. 8, pp. 1237–1243, 2012.

[61] Y. Ohmura, Y. Kuniyoshi, and A. Nagakubo, "Conformable and scalable tactile sensor skin for curved surfaces," in *Proc. IEEE Int. Conf. Robot. Autom (ICRA)*, 2006, pp. 1348–1353.

[62] E. del Sol, R. King, R. Scott, and M. Ferre, "External force estimation for teleoperation based on proprioceptive sensors," *Int. J. Adv. Robot. Syst.*, vol. 11, no. 3, p. 53, 2014.

[63] A. Wahrburg, E. Morara, G. Cesari, B. Matthias, and H. Ding, "Cartesian contact force estimation for robotic manipulators using Kalman filters and the generalized momentum," in *Proc. IEEE Int. Conf. Autom. Sci. Eng. (CASE)*, 2015, pp. 1230–1235.

[64] K. O. Hill and G. Meltz, "Fiber Bragg grating technology fundamentals and overview," *J. Lightwave Technol.*, vol. 15, no. 8, pp. 1263–1276, 1997.

[65] A. G. Leal-Junior, A. Theodosiou, C. Marques, M. J. Pontes, K. Kalli, and A. Frizera, "Compensation method for temperature cross-sensitivity in transverse force applications with FBG sensors in POFs," *J. Lightwave Technol.*, vol. 36, no. 17, pp. 3660–3665, 2018.

[66] A. Rajabzadeh, R. Heusdens, R. C. Hendriks, and R. M. Groves, "Calculation of the mean strain of smooth non-uniform strain fields using conventional fbg sensors," *J. Lightwave Technol.*, vol. 36, no. 17, pp. 3716–3725, 2018.

[67] R. C. Hibbeler, *Mechanics of Materials*, 8th ed. Upper Saddle River, NJ, USA: Pearson Prentice Hall, 2011.

[68] O. Khatib and J. Burdick, "Motion and force control of robot manipulators," in *Proc. IEEE Int. Conf. Robot. Autom. (ICRA)*, vol. 3, 1986, pp. 1381–1386.

[69] H. Seraji, "Adaptive admittance control: an approach to explicit force control in compliant motion," in *Proc. IEEE Int. Conf. Robot. Autom. (ICRA)*, vol. 4, 1994, pp. 2705–2712.